Seventh International Conference on
Computational Fluid Dynamics (ICCFD7),
Big Island, Hawaii, July 9-13, 2012

ICCFD7-4306

Inviscid Analysis of Extended Formation Flight

James Kless*, Michael J. Aftosmis**, S. Andrew Ning***, and Marian Nemec*
Corresponding author: james.kless-1@nasa.gov

* Science and Technology Corporation, Moffett Field, CA, USA.
** NASA Ames Research Center, Moffett Field, CA, USA.
*** Stanford University, Stanford, CA, USA.

Abstract: Flying airplanes in extended formations, with separation distances of tens of wingspans, significantly improves safety while maintaining most of the fuel savings achieved in close formations. The present study investigates the impact of roll trim and compressibility at a fixed lift coefficient on the benefits of extended formation flight. An Euler solver with adjoint-based mesh refinement combined with a wake propagation model is used to analyze a two-body echelon formation at a separation distance of 30 spans. Two geometries are examined: a simple wing and a wing-body geometry. Energy savings, quantified by both formation drag fraction and span efficiency factor, are investigated at subsonic and transonic speeds for a matrix of vortex locations. The results show that at fixed lift and trimmed for roll, the optimal location of vortex impingement is about 10% inboard of the trailing airplane's wing-tip. Interestingly, the improvement in drag fraction is relatively robust in the vicinity of the optimal position. Over 90% of energy benefits can be obtained with a 5% variation in vertical and 10% variation in spanwise positions. Control surface deflections required to achieve roll trim reduce the benefits of formation flight by 3-5% at subsonic speeds and 9-11% at transonic speeds. Overall, simulations show peak induced drag saving for the trail aircraft are 54% in subsonic flow and 35% in transonic flow while accounting for trim.

Keywords: Extended Formation Flight, Computational Fluid Dynamics, Wake Modeling, Compressibility, Trim.

Nomenclature

α	= angle of attack, deg
AR	= wing aspect ratio
b	= aircraft wingspan
c	= local chord
c_{avg}	= average chord
C_L	= lift coefficient
$C_{L\alpha}$	= lift-curve slope
C_l	= sectional lift coefficient
C_D	= drag coefficient
C_{Di}	= inviscid drag coefficient
C_m	= pitching Moment (with respect to c.g.)
C_P	= pressure coefficient
e	= span efficiency factor $(C_L^2/(\pi * AR * C_{Dinviscid}))$
M_∞	= free-stream Mach Number
y	= lateral vortex position relative to wingtip
z	= vertical vortex position relative to wingtip

1   Introduction

Formation flight has been studied extensively by biologists and aerodynamicists for its significant energy savings. A trailing aircraft flying in the upwash region of the outboard wingtip vortices left by the leading aircraft experiences a forward tilted lift vector which, effectively reduces the induced drag of the trailing aircraft while simultaneously increasing its lift. As a result, the trailing aircraft can fly at a lower angle of attack than the lead aircraft while still maintaining the same lift, resulting in decreased energy expenditure. In nature, migrating birds have exploited these energy savings extensively. Lissaman and Shollenberger[1] theoretically showed that 25 birds flying in formation could achieve a range increase of 70 percent as compared to a single bird. Similarly, Hainsworth[2] estimated a 36% induced power savings (about half of the maximum achievable) for a flock of 55 geese. Further studies by Hummel[3, 4] have verified these claims and developed methods for estimating the induced drag savings.

Flight tests have been performed on conventional aircraft where similar savings have been found. In Wagner et. al. [5], T-38 aircraft flying in formation were used at different formation positions to determine which was optimal. It was concluded that fuel savings of 8.8% were achieved in the optimal position. Vachon et. al. [6] conducted a similar study with F/A-18 aircraft flying in close formation. Calculations revealed that a 20% drag reduction and 18% fuel flow reduction was achieved. More recently, analytical methods have been used to quantify the benefits of formation flight[7] for commercial transport and route optimization.

While close formation flight is highly appealing for UAVs and fighter jets, commercial jets and military transport vehicles are constrained by FAA requirements on streamwise separation. Therefore, a more practical approach for these aircraft is flying in extended formations to avoid collisions and wake turbulence. Ning et al.[8] explored the benefits of extended formation flight by examining effects such as wake roll-up, vortex decay, vortex instabilities, vortex motion, and atmospheric turbulence. These studies concluded that for streamwise separation of less than 20 spans, a two-aircraft formation achieves a reduction of 26-31% in induced drag, while a three-aircraft formation obtains a 38-45% reduction. These preliminary studies were based on incompressible flow models, hence for practical applications the effects of compressibility remain an open question.

In addition to compressibility, a second concern with practical formation flight is the degradation of benefits due to trimming the trailing aircraft with existing control surface designs. The potentially large rolling moments produced by the leading aircraft's wingtip vortices presents a challenge in determining proper positioning of the trailing aircraft. As has been showed by Ning[9], typically the trail positions that lead to greatest induced drag benefits also tend to produce the greatest induced rolling moments requiring greater control surface deflection to trim. This becomes increasingly important at transonic speeds as the drag penalty to trim may be compounded by compressibility.

The present study uses NASA's inviscid AERO package[10, 11, 12, 14, 15, 16] in conjunction with a vortex propagation technique to examine two different geometries; a low-speed extruded NACA 0012 wing, and a transonic wing-body geometry. The objective of the current work is to quantify the effects of trim and compressibility on formation flight performance at fixed lift coefficient for an extended two-craft echelon formation. An iterative approach to roll trim the aircraft at a specified lift coefficient is presented. Additionally, the methodology developed will provides a building block for increasing fidelity of aircraft geometries in extended formations.

2   Methods

2.1   Modeling Procedure

In close formation flight, aircraft are separated by only a few spans and there is a symbiotic relationship among the aircraft. Not only does the lead aircraft influence the followers, but the followers reduce the drag on the lead as well. Simulations of close formation flight, therefore require mechanisms for coupling the flight mechanics and aerodynamics of all the aircraft in formation. In extended formation flight, we consider aircraft separated by 15-40 spans. With such large separations, the influence of the trailing aircraft on the leader becomes negligible. This decoupling leads to a natural separation of the problem into three phases: (1) simulation of the lead aircraft in free air; (2) propagation of the lead aircraft's wake/vortex system and (3) simulation of the trailing aircraft with the aged wake/vortex at the inflow boundary.

Figure 1 lays out the basic modeling paradigm. An inviscid solution is obtained on the lead aircraft at the designed cruise C_L. A lift distribution is extracted from the solution and propagated using the augmented Betz method as described in Ning[9, 13]. This method uses far-field conservation of vorticity combined with empirical data to rollup the wake and then applies LES decay rates to age the vortex as it convects downstream.
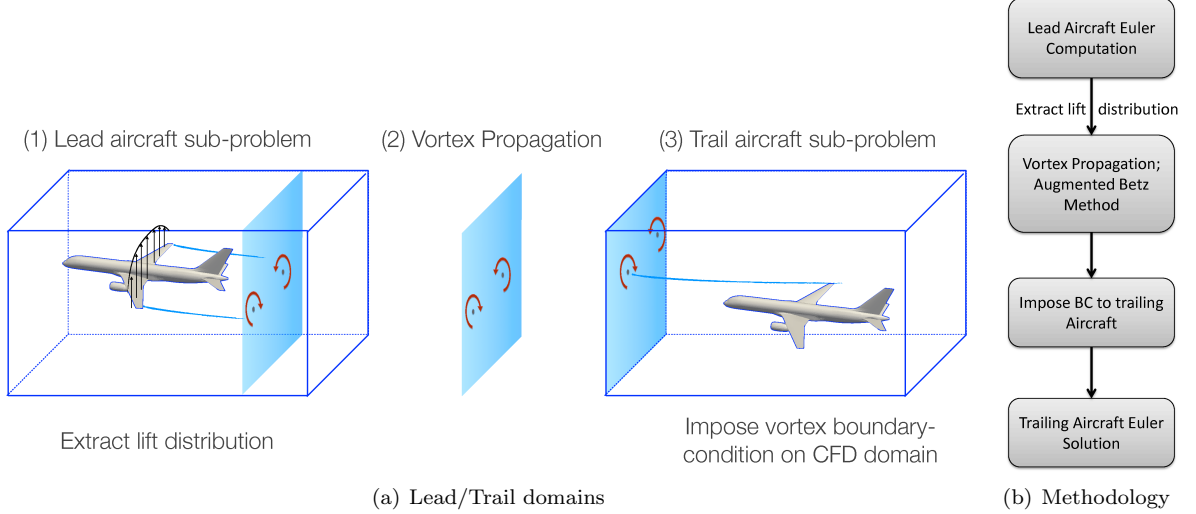

(a) Lead/Trail domains   (b) Methodology

Figure 1: Complete modeling procedure to extract lead aircraft CFD results, propagate vortex, and impose a modeled vortex as the inflow boundary condition for the trailing aircraft domain.

After propagation (30 spans for the current study), the vortex is modeled by a piecewise analytic solution which is imposed on the inflow plane of the trailing aircraft domain. A domain size sensitivity study was conducted to determine the proper streamwise distance upstream of the aircraft to impose the boundary condition. Distances of five, eight, and ten spans upstream of the geometry were tested in mesh convergence studies. Eight spans was selected due to negligible sensitivity to boundary location while reducing the computational cost. The angle of attack of the trailing aircraft is adjusted to match the C_L of the lead aircraft and control surfaces may be deflected to trim the aircraft in roll as well. The solution strategy is depicted in Fig. 1 (a) with a corresponding flowchart in Fig. 1 (b).

2.2   Flow Analysis

All simulations are performed with the NASA's AERO analysis package[10, 11, 12, 14, 15, 16], which uses the three-dimensional Euler equations of a perfect gas to model the flow. The equations are discretized using a second-order, cell-centered, finite-volume scheme based on van Leer's flux vector splitting and limiter. Steady-state solutions are obtained through the use of multigrid-accelerated five-stage Runge-Kutta scheme in conjunction with domain decomposition for parallel computing. The computational mesh consists of Cartesian hexahedra everywhere, except for a layer of body-intersecting cells, or cut-cells, adjacent to the vehicle surface. Meshes are constructed via an adaptive mesh refinement procedure that uses the method of adjoint-weighted residuals to estimate discretization errors in selected output functionals. In this work, the output functional in all computations is the span efficiency factor, e, given by equation 1.

$$e = \frac{C_L^2}{\pi\,AR\,C_{Di}} \tag{1}$$

A typical computation involves about eleven mesh refinement cycles, starting from a coarse mesh of about 100,000 cells. During each refinement cycle, the number of cells in the mesh is increased by a prescribed growth factor. Small growth factors, e.g. 1.1, are used in the early refinement cycles to minimize computational work while reducing the discretization errors with the greatest influence on span efficiency. To further reduce computational work, we take advantage of the decoupling of the streamwise and crossflow velocities

in the incoming vortex. The initial mesh is constructed with stretched cells (aspect ratio of eight) in the streamwise direction in the region between the inflow boundary and the airplane, while isotropic cells are used near the airplane itself. This allows both efficient propagation of the vortex from the inflow boundary to the airplane and accurate computation of the flowfield near the airplane.

2.3   Trim Strategy

In contrast to previous work from Bower et. al.[7], which modeled trim with lower fidelity methods such as vortex-lattice schemes, the current work uses an iterative approach with higher fidelity numerical simulations. The process of trimming the trail aircraft in roll while maintaining constant C_L is completed in several steps.

The process begins by computing a flow solution on the trailing aircraft, where the freestream velocity vector is aligned with the streamwise coordinate of the Cartesian mesh. The flow solution is computed with the freestream velocity vector aligned with the streamwise coordinate of the Cartesian mesh. This implies that the angle of attack is specified via a rotation of the entire aircraft relative to the computational domain. The lift and rolling moment values are extracted and compared to their target values. The angle of attack and aileron deflection angle are iterated by using an under-relaxed Newton iteration with pre-computed values for $C_{L\alpha}$, and aileron roll authority. The aileron components are rotated with respect to the geometry using the Geometry Manipulation Protocol (GMP) library[17] to obtain a new wetted surface using Boolean solid operations. The new geometry is then rotated to the new angle of attack and the domain is automatically re-meshed. This process repeats until a convergence criterion is met. The convergence tolerances for these cases were 0.0012 for C_L and 0.00015 for rolling moment coefficient. Figure 2 gives a block-diagram abstraction of the approach.
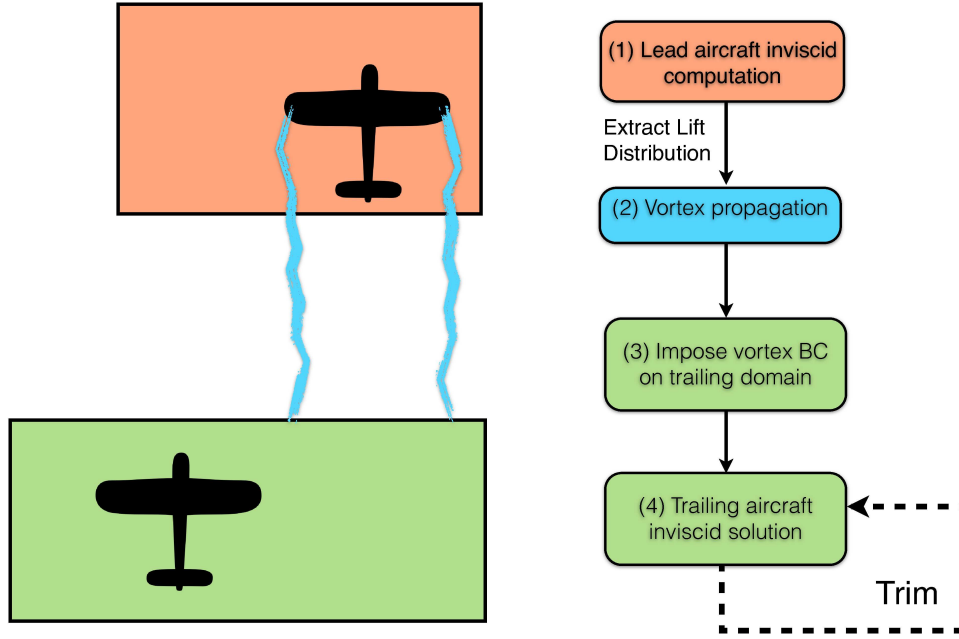

Figure 2: Flowchart depicting trim strategy. (1) A lead aircraft inviscid solution is computed from which the lift distribution is extracted and used as the initial condition for (2) analytic vortex propagation. (3) The vortex BC is imposed on the trailing aircraft domain. (4) Trailing aircraft inviscid solution is computed. Trim at fixed lift is accomplished through Newton iteration using pre-computed values of $C_{L\alpha}$ and roll authority.

Each trim iteration requires computation of a mesh adapted solution with about 10 adapt cycles with the final mesh reaching around 8 million cells. Typically, trim conditions were nearly met after about 5-6 trim iterations on these coarser meshes. Finally, an additional 2 or 3 higher resolution flow solves (about 16 million cells, 11 adapt cycles) was required to trim the aircraft within the tolerances. Each coarser trim iteration required roughly 150 CPU-hours on the 1.6 GHz Intel Itanium processors of the Columbia Supercomputer at

NASA Ames Research Center. The higher resolution flow solves each required roughly 300-400 CPU-hours. Therefore, the total computational cost of one flight condition was roughly 1400 CPU-hours.

3 Results

A verification study on vortex propagation is presented first to demonstrate the correctness and effectiveness of the mesh refinement procedure. Thereafter, results are presented for both a subsonic simple wing and a transonic wing-body geometry arranged in a two-aircraft echelon formation. Since there is no wave drag in the subsonic example, results for the simple wing may be compared with those from engineering methods to corroborate mesh converged solutions. This wing will also be used to demonstrate the effect of trim on performance in the absence of shocks. Simulations with the transonic wing-body configuration take these investigations further by including both the effects of compressibility and more realistic geometry on the drag savings.

The final force and moment values were obtained by performing Richardson extrapolations[18] of each coefficient. Simulations with poor error convergence in later adaption cycles were corrected by using earlier, well-behaved adaption cycles in the Richardson extrapolation. Our metrics of interest used to quantify benefits of formation flight are the span efficiency factor, (Eqn. 1), and formation drag fraction which represents the sum of the induced drag of all aircrafts in formation versus the induced drag of all aircrafts out of formation:

$$\text{drag fraction} = \sum D_{i,formation} / \sum D_{i,out-of-formation} \qquad (2)$$

3.1 Vortex Propagation within the CFD Domain

In order to quantify resolution requirements for accurately propagating the vortices within the trail aircraft computational domain, a mesh convergence study was performed. To do this, the aircraft geometry was taken out of the domain and the vortices were propagated 5 spans (roughly 400 core diameters) downstream from the inflow boundary. Mesh adaptation was driven by a pressure integration on a line at 5 spans downstream from the inflow plane. Fig. 3. depicts the scenario.

This study gives confidence that when the trail aircraft is included, the mesh adaption strategy will ensure it sees an accurate representation of the oncoming vortices. Fig. 4 displays cutting planes (constant x) at the inflow, and 5 span locations. The corresponding line sensors through the vortex cores are shown. Although both wingtip vortices are computed, only the vortex closest to the sensor is being shown. In addition, the descent of the vortex core is visible and appears to descend 1 core diameter over the 5 spans, consistent with the analytic prediction of the Biot-Savart Law.
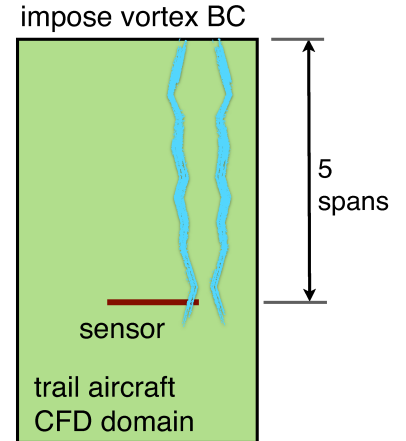

Figure 3: Top-down view of trail aircraft domain depicting vortex entering domain. Mesh adaptation was driven by a pressure integration on a line at 5 spans downstream from the inflow plane.
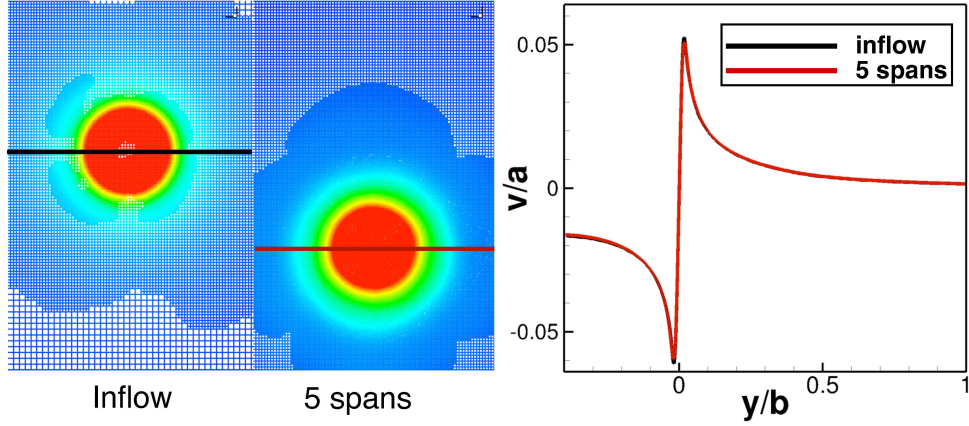
Figure 4: From left to right. A cross sectional cut of the inflow plane is shown with a line sensor through the core depicting pressure contours. At 5 spans downstream, the same cut is taken with a corresponding line sensor through the core. Finally, the upwash as a function of span is plotted for both the inflow and dowstream stations.

Comparing the upwash as a function of span at the two locations, we see excellent agreement between the inflow, and downstream locations. It is clear that we are recovering almost all of the upwash at 5 spans (400 core diameters). Fig. 5 (a) displays the mesh convergence history for the objective functional (in this case, the pressure integration on the line sensor placed 5 spans downstream from the inflow plane). The sequence of adapted meshes generates converging functional estimates, with essentially no change for the final two meshes. Moreover, the adjoint-based error estimate, shown in (b) displays a decrease in error (on log-log scale) as the cell count increases thereby reinforcing mesh convergence of the simulation.
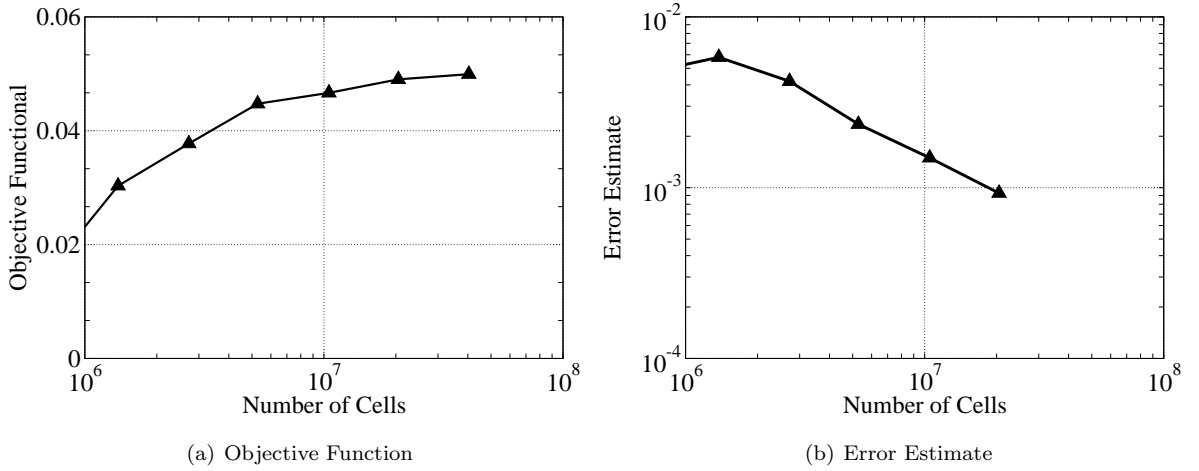

(a) Objective Function

(b) Error Estimate

Figure 5: Mesh convergence on flow in empty domain. (a) line pressure sensor convergence, (b) convergence error estimate.

3.2 Simple NACA 0012 Wing

The first case considers a low-speed wing with an aspect ratio of 8, NACA 0012 cross-sections, a smooth end cap, no sweep and no taper. Figure 6 shows the wing along with the ailerons.

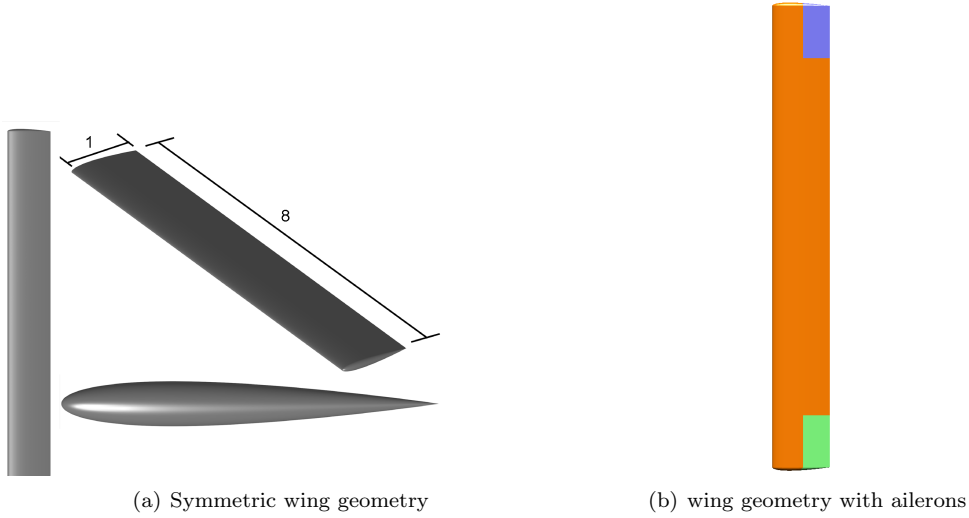(a) Symmetric wing geometry   (b) wing geometry with ailerons

Figure 6: A simple NACA 0012 wing with aspect ratio of 8: (a) isometric view without ailerons. (b) a planform view depicting the spanwise and chordwise extent of the ailerons.

The ailerons of the NACA 0012 wing extend from the wingtip to 20% semispan inboard and from the trailing edge upstream 50% chord. Computations for the wing were made at a constant $C_L = 0.55$, and $M_\infty = 0.5$. Three separate trim configurations are examined. The first is the baseline, or un-trimmed configuration with no aileron deflections. The second configuration trims the aircraft by deflecting a single aileron opposite the incoming vortex. This is the simplest trimming strategy in that it increases the lift on the out-of-vortex wing, allowing the same net lift to be achieved at a lower angle of incidence. Finally, the third configuration, referred to as the "two-aileron trimmed configuration", trims the aircraft in the conventional manner by deflecting both ailerons by equal amounts in opposite directions. The three trim configurations are shown schematically in Fig. 7. We consider trim using conventional ailerons rather than more futuristic trimming strategies since they can be implemented in today's aircraft without modification.
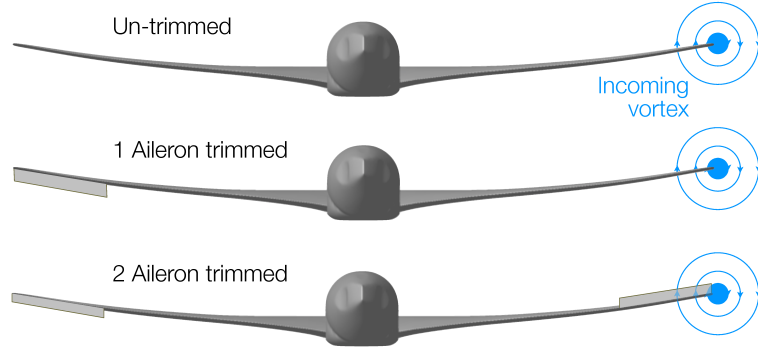

Figure 7: Schematic depicting trim configurations as viewed from behind the trailing aircraft. The incoming vortex is positioned near the pilots right wingtip.

The adjoint-based error estimate provided by the simulation package provides direct assessment of mesh convergence, or mesh sensitivity of the flow solution. By tracking the error estimate and output functional evolution, the degree of mesh convergence can be discerned. Functional convergence along with error estimate for a representative case are shown in Fig. 8. This particular case was run for 11 mesh adaption cycles with the final mesh reaching about 20 million cells. Fig. 8 (a) shows the functional is approaching a value of close to 1.52. The flattening of the functional curve with additional refinement indicates mesh convergence. Fig. 8 (b) displays the adjoint estimate of the bound on the error in span efficiency factor. On the initial coarse meshes, low error is estimated as the flow around the body has not been established due to under-resolution. As the refinement progresses, the error-estimate improves revealing higher, but more credible,

error predictions. Further refinement drives down this error by attacking areas of the flow that contribute most to the discretization error on span efficiency factor.
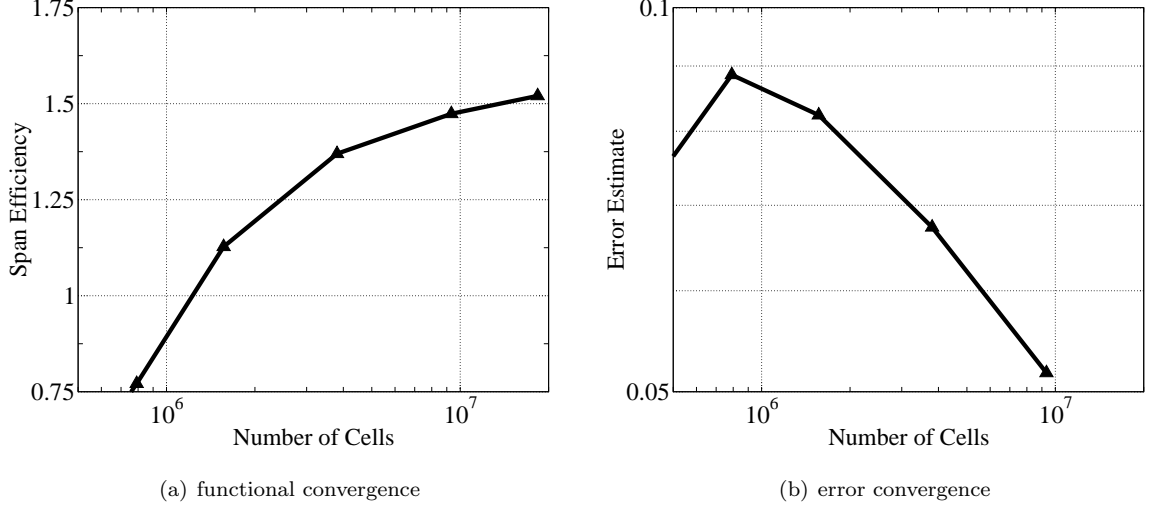

(a) functional convergence

(b) error convergence

Figure 8: (a) Functional convergence along with (b) adjoint-based error estimate for a representative case. Ater 11 adaption cycles the error is reduced, while the functional is flattening. The final continuum value of span efficiency is achieved by performing a Richardson Extrapolation using the final two adaptions.

Fig. 9 displays the initial and final adapted meshes for a representative case for two different views. The initial mesh consisted of around 100,000 cells, while the final mesh contained around 20 million. The initial mesh included streamwise cell stretching in the region between the wing and the inflow boundary. The final mesh (Fig. 9 (b) and (d)) shows high refinement around the wing, in addition to the refinement of both incoming vortices tracked all the way to the inflow plane. The finest cells on the wing are roughly three to four adaptions finer than those in the vortex. The high aspect ratio streamwise stretching is evident in the vortex propagation region of Fig. 9.

(a) initial mesh, far-view   (b) final mesh, far-view

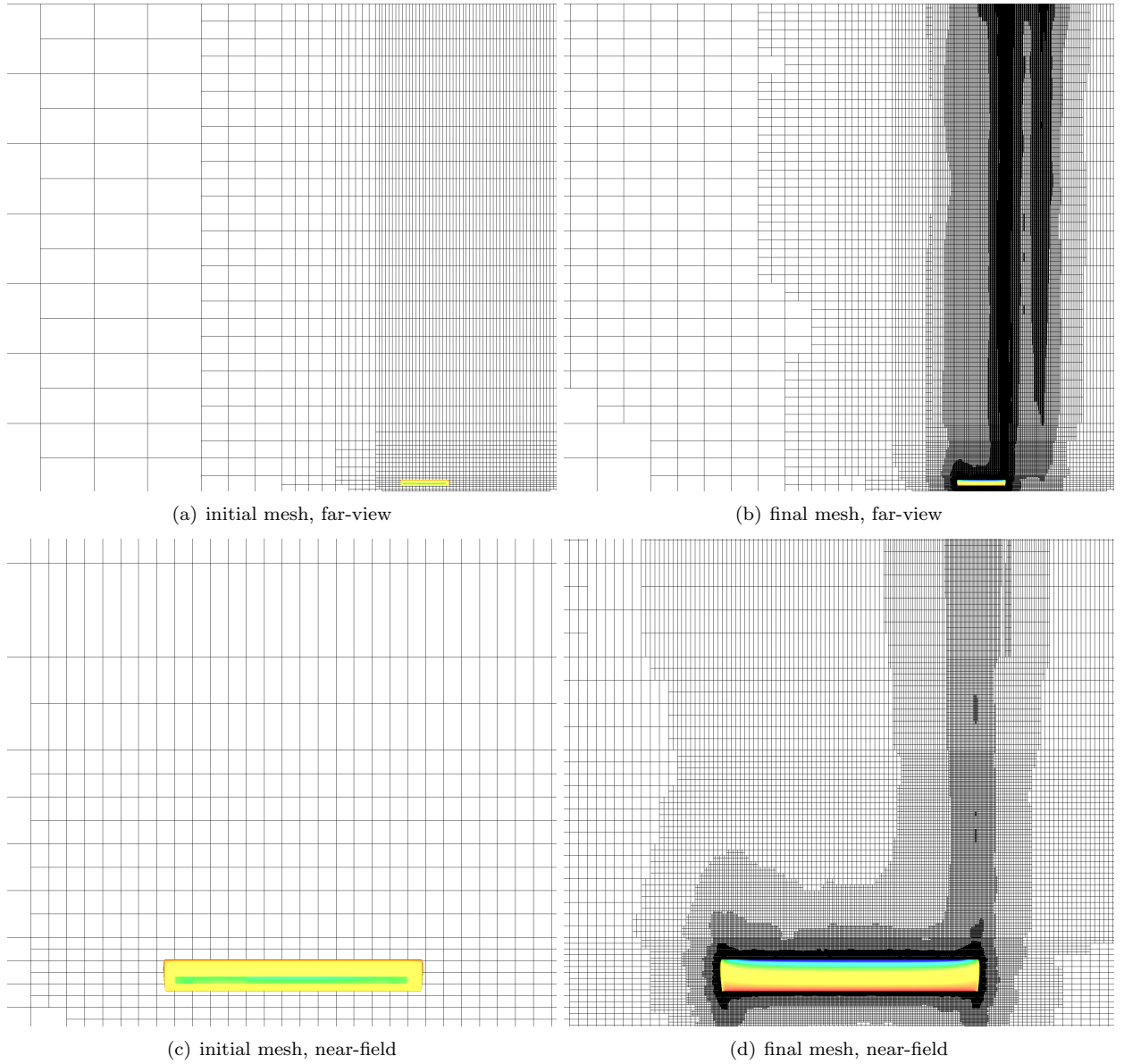(c) initial mesh, near-field   (d) final mesh, near-field

Figure 9: Initial and final adapted meshes after 11 adapt cycles. The initial mesh consisted of about 100,000 cells, while the final mesh contained 20 million. C_P contours are seen on the surface of the wing. Streamwise cell stretching up to aspect ratio of eight can be seen upstream of the wing.

Fig. 10 displays the incoming vortices approaching the trail wing. Mesh adaption refines the wing surface grid as well as attacking the error associated with the incoming vortices, as both have an effect on the span efficiency factor. The adaptation refines the vortex 8 spans (64 chords) upstream to the inflow boundary. Fig. 10 (a) shows the incoming vortex core highlighted by contours of streamwise vorticity, while Fig. 10 (b) highlights the near-body refinement.
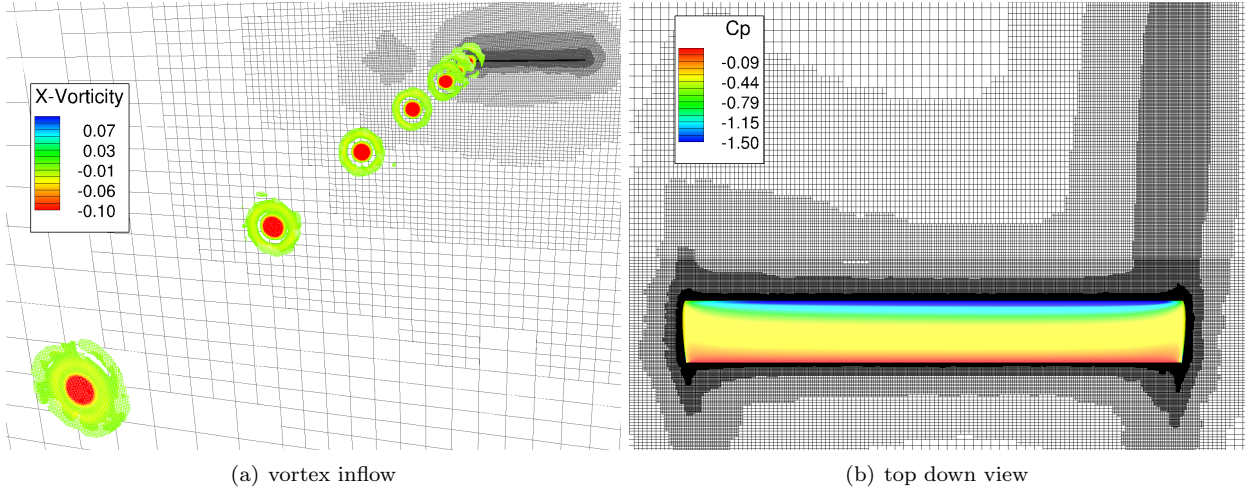
9

(a) vortex inflow

(b) top down view

Figure 10: (a) X-vorticity contours depict the incoming vortex on the trail aircraft. A cutting plane at the trailing edge is also shown to display the mesh adaption. The other wingtip vortex is blanked out for ease of visualization. (b) planform view of the wing colored by pressure coefficient. Mesh refinement proceeds around the body as well as upstream to the inflow plane to capture the incoming vorticies.

3.2.1 Vortex Position Sensitivity

A matrix of incoming vortex positions was used to create a map of drag savings and study the sensitivity of drag savings to the location of vortex core with respect to the wingtip at the leading edge plane. Fig. 11 shows the coordinate system along with the run matrix. The origin of the coordinate system is at the wingtip. For consistency, all spanwise loading plots will use this coordinate system. The spanwise domain extended from 20% of wingspan inboard ($y/b = -0.2$) to 30% of wingspan outboard ($y/b = 0.3$) of the wingtip. The vertical domain extended from 10% below the wing to 10% above the wing. Individual data points can be seen in the figure. Each data point represents a trim-converged solution depending on the configuration used. A typical simulation used about 20 million cells. For this study, the three trim configurations discussed earlier were used, each containing 25 data points for a total of 75 cases.
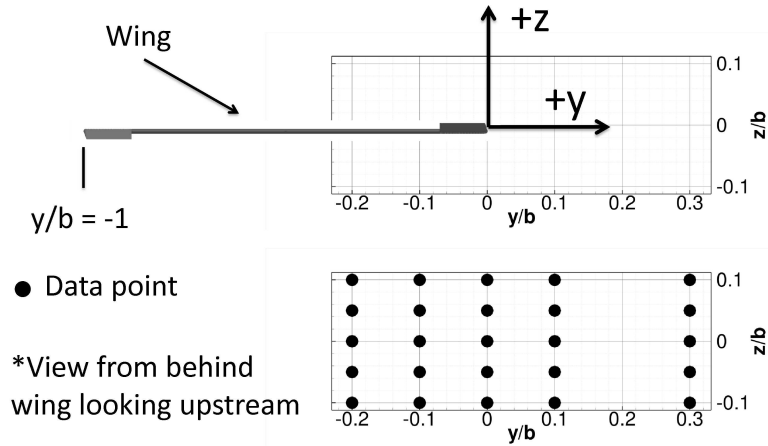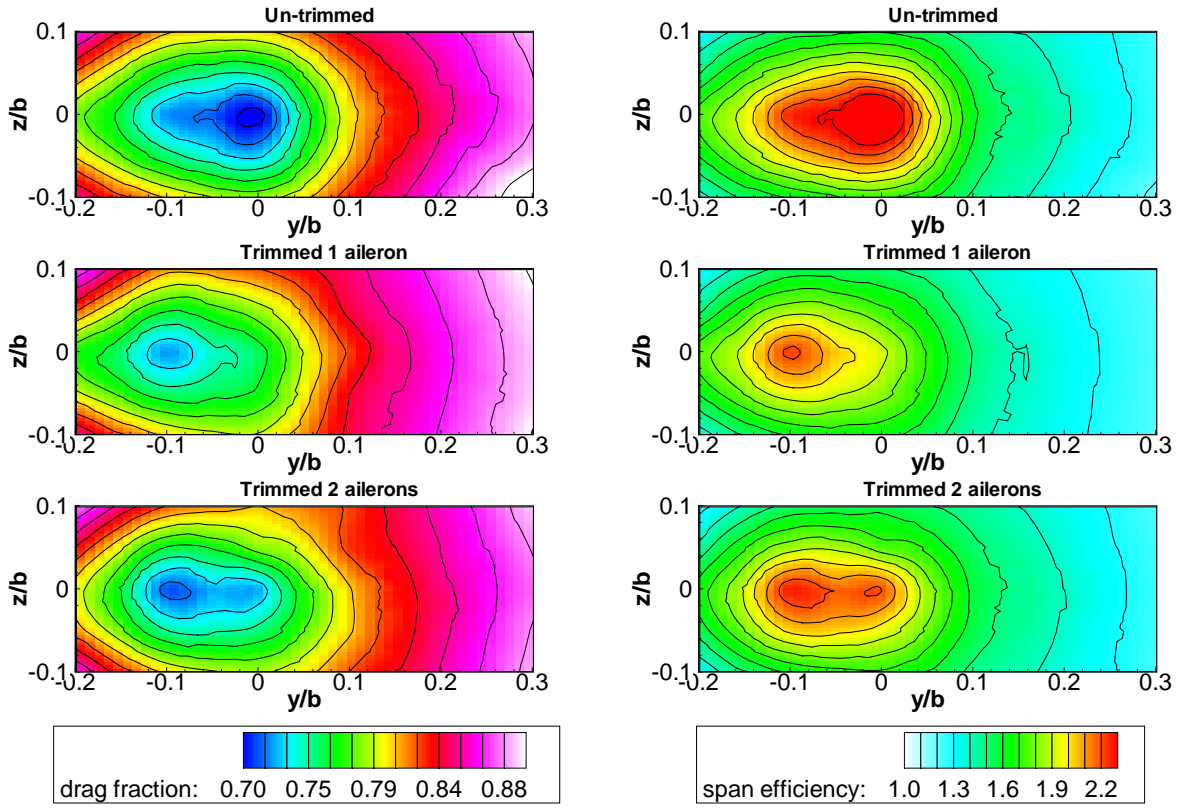

Figure 11: Vortex position with respect to trail aircraft wingtip. The view is taken from behind the trail aircraft facing upstream. The left wingtip begins at a $y/b = -1$ and the right wingtip ends at $y/b = 0$.

Results for the three trim configurations were fit using a Kriging surface and contoured. Fig. 12 shows results for drag fraction and span efficiency factor. For the un-trimmed configuration, the highest drag savings appears to be at the wingtip with slight overlap achieving drag fractions of about 0.7. The trends

10

and optimal values show strong quantitative agreement with the vortex lattice-based positioning study presented in Ning [9]. Optimal values in both studies show drag fractions of about 0.7 occuring near the wingtip. In addition, both studies reveal that near the optimal positions, the drag savings is much more sensitive to vertical position as opposed to lateral positioning. Overall, close agreement with the vortex lattice-based solver confirms accuracy of the simulations.

Trimming the aircraft with either one or two ailerons moves the optimal vortex position to about 10% inboard of the tip ($y/b = -0.1$). In addition, the one-aileron trimmed configuration produces less drag savings, while the two-aileron trimmed configuration produces a significant improvement in drag fraction. In general, sub-critical trim accounts for a 3-5% increase in formation inviscid drag fraction and 8-10% decrease in span efficiency factor. In terms of drag savings on the trail wing alone, a 60% savings in induced drag is achieved without accounting for roll-trim, while a 54% savings in induced drag is achieved with trimming in roll at sub-critical flight conditions. Therefore, roll-trimming in sub-critical flight conditions accounts for a 6% erosion of formation flight inviscid drag savings on the trailing aircraft.
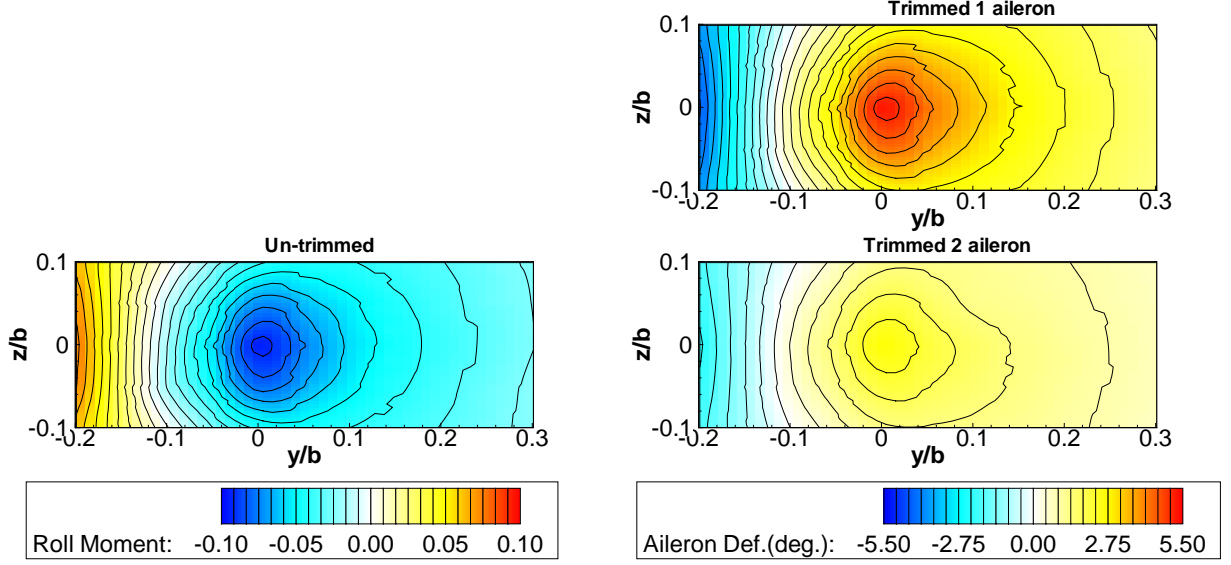

(a) drag fraction   (b) span efficiency factor

Figure 12: Contour maps for (a) drag fraction and (b) span efficiency factor. The highest drag savings occur when the vortex is near the wingtip with slight overlap for the un-trimmed configuration, and migrates inboard (near $y/b = -0.1$) for the two trimmed configurations. In addition, the radius of the optimal location shrinks significantly for the one aileron trimmed configuration.

Interestingly, the entire region covered by the contour plots in Fig. 12 produces at least an 8% drag fraction savings for the two-aircraft formation. Near the optimal location, the un-trimmed configuration experiences a roughly 30% reduction in drag fraction for the formation.

Figure 13 displays contour plots of rolling moments along with corresponding aileron deflection angles. The largest rolling moments occur when the vortex is at around the $y/b = -0.2$ and $y/b = 0$ span locations, with a sign change undergone at around $y/b = -0.1$. This sign change is a result of the outboard portion of the wing experiencing greater downwash, and larger upwash further inboard. As expected, trimming with

only one aileron requires roughly twice the aileron deflection angle as the two aileron case. In addition, the rolling moment and aileron deflection contours lend insight into why the optimal vortex location migrates inboard with trim. At the wingtip, since the rolling moments are at a maximum, the corresponding aileron deflections are also at a maximum incurring the highest trim penalty. Inboard, close to $y/b = -0.1$ where there are small rolling moments, the aileron deflections required to trim are also small incurring the smallest trim penalty.

(a) rolling moment coefficient

(b) aileron deflection to trim

Figure 13: (a) Rolling moment coefficients along with corresponding (b) aileron deflection angles. The largest rolling moments seem to occur at the -20% overlap position and at the wingtip. The rolling moment changes sign as the vortex moves inboard as the wingtip within the vortex experiences more downwash and larger upwash inboard.

Fig. 14 displays spanwise lift distributions for five different lateral vortex locations all at a fixed vertical position at the wing tip. As the vortex moves inboard from $y/b = 0.3$ of the span, larger and larger modulations are seen. The two-aileron configuration retains a more symmetric lift distribution than the 1 aileron case, leading to higher span efficiencies as seen in the contour plots. At $y/b = -0.1$ inboard, the shift in aileron deflection becomes discernible as the rolling moment changes sign.
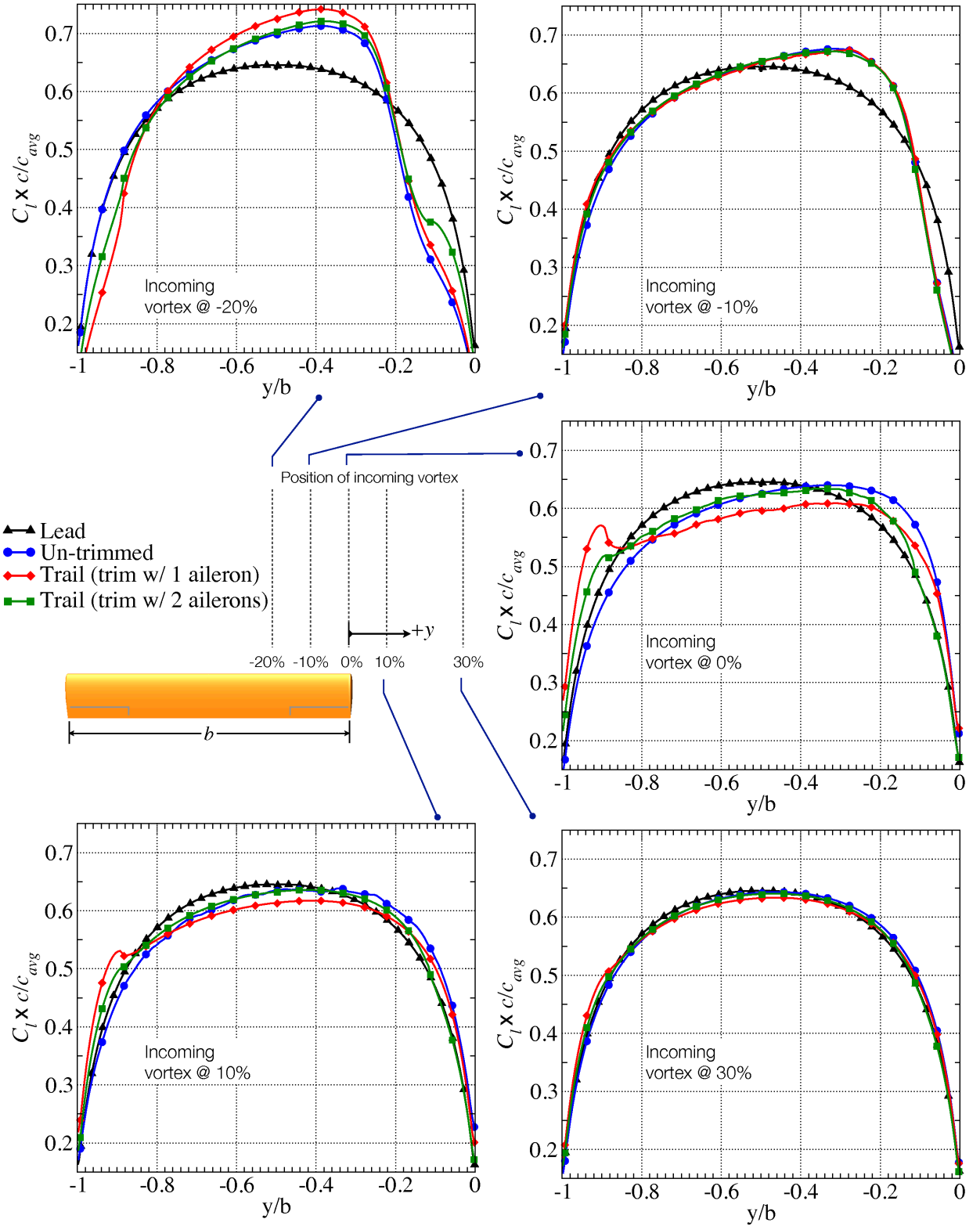
Figure 14: Spanwise load distributions for constant vertical position at $z = 0.0b$.

Figs. 15, 16, 17 show spanwise load distributions for 5 lateral vortex positions at a given configuration at two different constant vertical positions. The most extreme modulations to the lift distributions occur at

inboard locations between $y/b = -0.1$ to $y/b = -0.2$ as the in-vortex wingtip experiences greater downwash. As the vortex is positioned further outboard, the lift distribution approaches its symmetric, out-of-vortex distribution. The one-trimmed configuration, Fig. 16, exhibits the most drastic lift distribution modulations relative to the other two configurations. This is a result of the aileron having to deflect to a larger angle to trim, thus disrupting the smooth distribution.
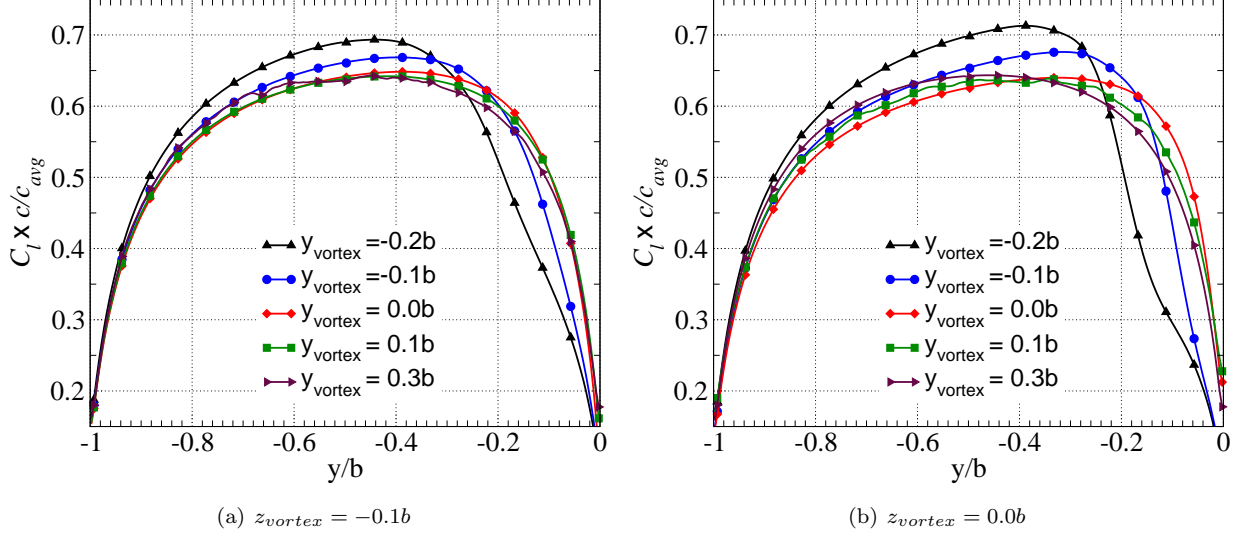

(a) $z_{vortex} = -0.1b$ (b) $z_{vortex} = 0.0b$

Figure 15: Spanwise lift distributions for un-trimmed wing. The most extreme modulations to the lift distributions occur when the vortex is at inboard locations between $y/b = -0.1$ and $y/b = -0.2$ as the in-vortex wingtip experience greater downwash.
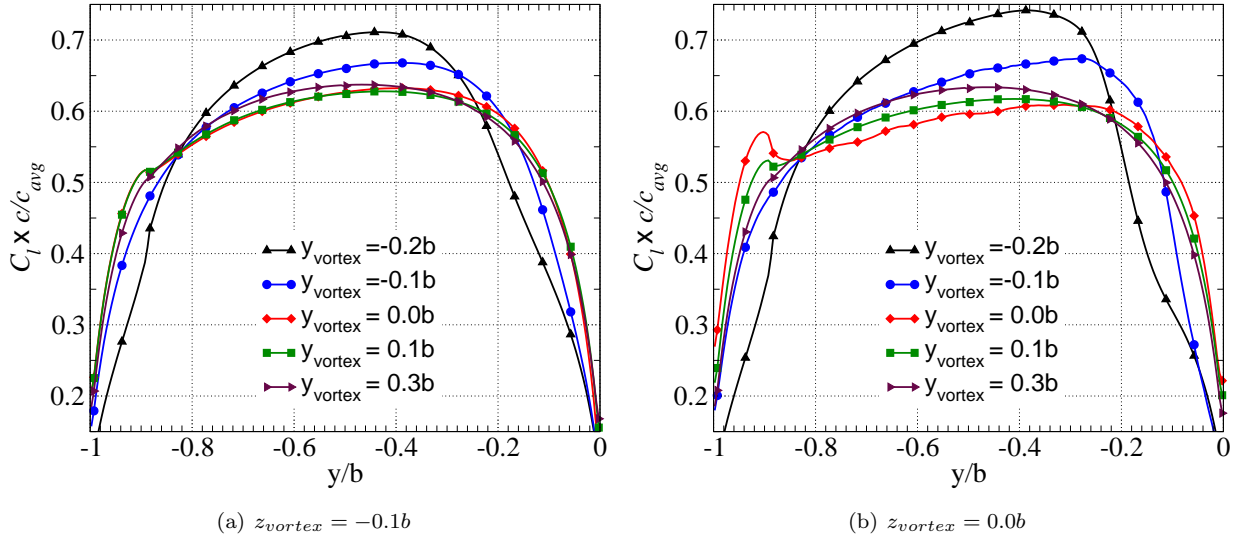

(a) $z_{vortex} = -0.1b$ (b) $z_{vortex} = 0.0b$

Figure 16: Spanwise lift distributions for one-aileron trimmed wing.

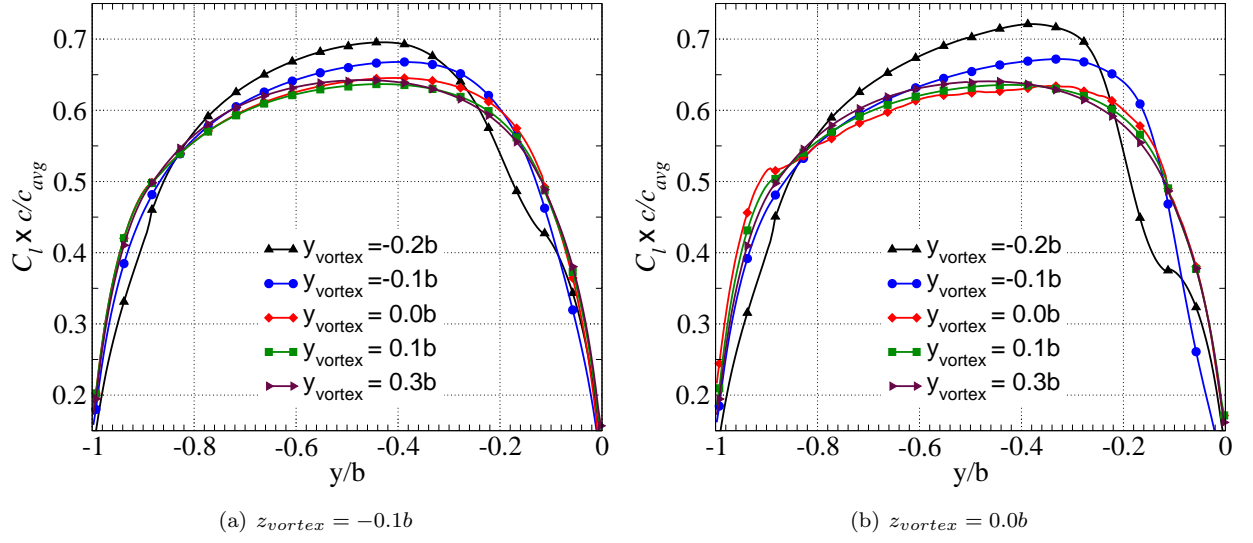(a) $z_{vortex} = -0.1b$ (b) $z_{vortex} = 0.0b$

Figure 17: Spanwise lift distributions for two-aileron trimmed wing.

3.3 Common Research Model

Having demonstrated the overall trim procedure on a simple geometry at sub-critical conditions, the goal is to analyze more realistic flight conditions. The wing-body geometry used for this study is shown in Fig. 18, and is based on the Common Research Model (CRM) geometry used in the 4th AIAA CFD Drag Prediction Workshop[19]. This model was chosen due to the large amounts of previous computational and experimental data.

(a) CRM geometry   (b) CRM geometry with ailerons
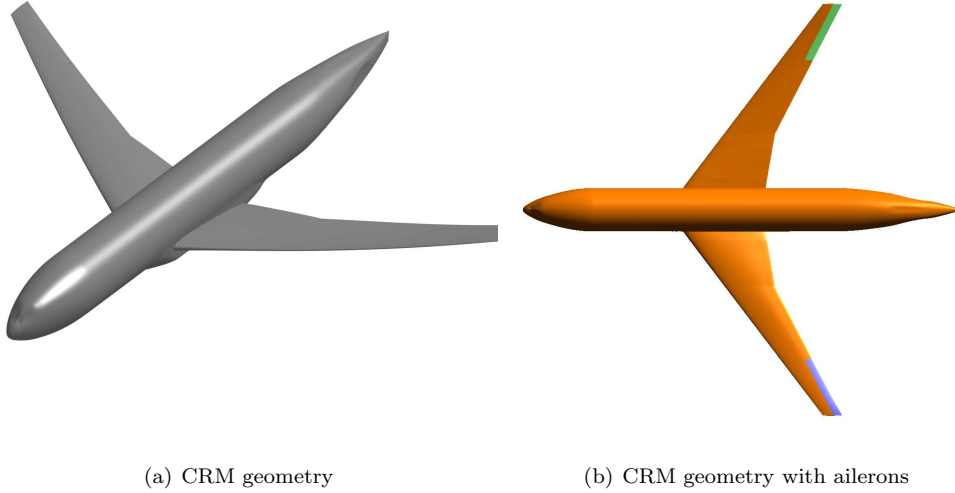
Figure 18: The CRM geometry used in the 4th AIAA CFD Drag Prediction Workshop[19] (a) Isometric view without ailerons. (b) a planform view depicting spanwise and chordwise extent of the ailerons.

The CRM ailerons extended roughly 15% of the span inboard from the wingtip and spanned roughly 50% to 15% of the chord. Based on the previous results for the wing, it was shown that the 2-aileron trim strategy out performed the 1-aileron strategy. Therefore, all trim computations for the CRM will use the 2-aileron strategy to trim. Fig. 19 displays an isometric view of the incoming vortex colored by x-vorticity magnitude. Cell stretching is seen upstream of the geometry along with refinement near the vortex core.

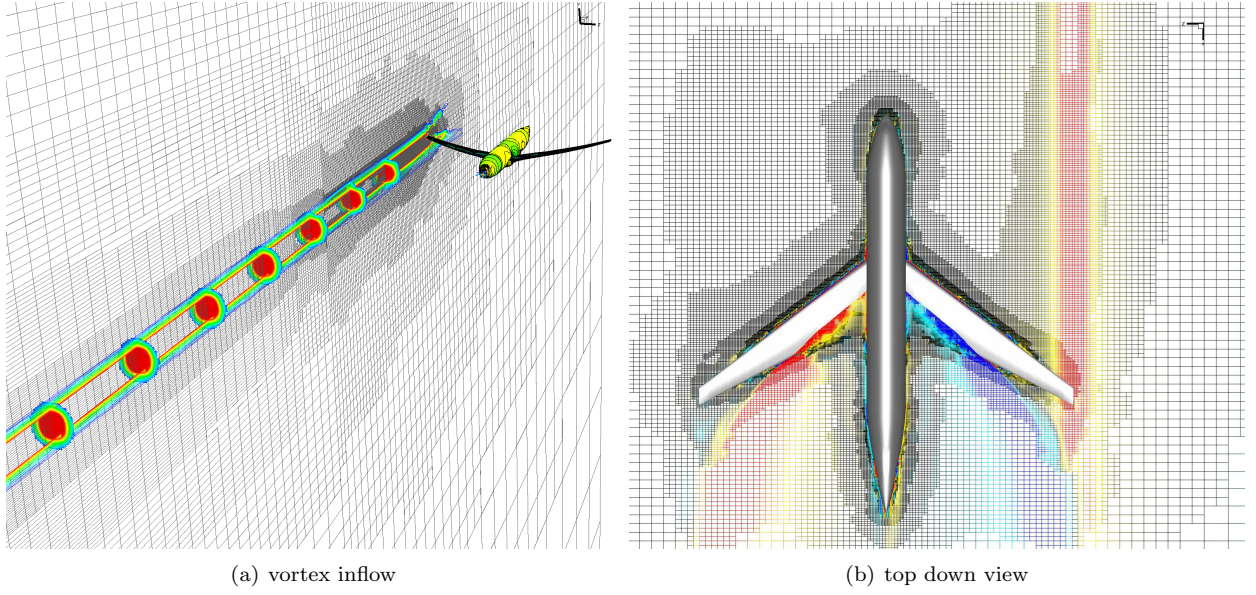(a) vortex inflow   (b) top down view

Figure 19: (a) streamwise vorticity contours depict the incoming vortex on the trail aircraft. The other wingtip vortex is not displayed. (b) planform view of the CRM colored by streamwise vorticity contours. Mesh refinement proceeds around the body as well as upstream to the inflow plane to capture the incoming vorticies.

3.4 Mach Number Sensitivity

A key component of transonic flight is the drag divergence which occurs at a critical Mach Number. Fig. 20 (a) shows sensitivity of inviscid drag to Mach Number at constant C_L of the wing-body CRM geometry. At Mach of 0.79, the wing is essentially shock free, and at 0.85 a strong shock sits on the aft section of the wing. Fig. 20 (b) gives the inviscid drag (on lead and trail aircraft) as a function of Mach Number at transonic conditions when the incoming vortex is positioned at the wingtip. Without trimming in roll, savings of nearly 50% in inviscid drag is achieved. When roll-trim is accounted for, this savings is decreased to about 35%. Overall, trim accounts for about a 15% erosion of formation flight benefits in transonic flight. In addition, this delta remains fairly insensitive to Mach Number for the range tested.

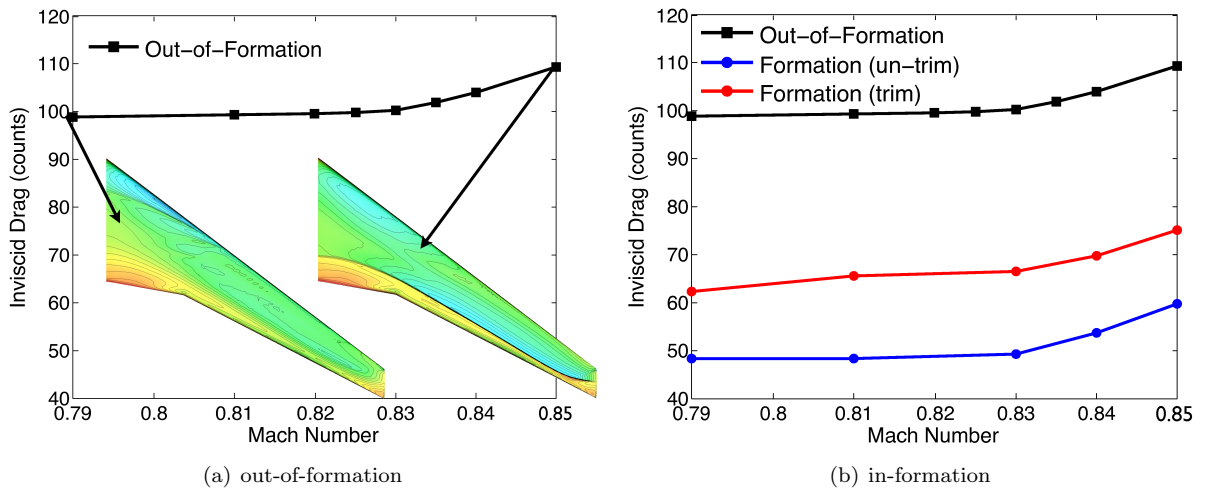(a) out-of-formation   (b) in-formation

Figure 20: (a) Mach sensitivity of CRM for out-of-formation flight (lead aircraft). At Mach of 0.79, the wing is essentially shock free, while at Mach of 0.85, a strong shock sits on the aft section of the wing. (b) Mach Sensitivity with roll-trim. Transonic trim accounts for about 15% erosion of formation flight benefits.

Figure 21 displays the in-vortex wing of the CRM at Mach Number of 0.83 for three different flight configurations; out-of-formation flight (lead aircraft), in-formation without roll-trim (un-trim), and in-formation with trim (trim). C_P distributions are shown on the wing at 50 and 90% semispan. At 50% semispan, the C_P distributions agree closely. However, at 90% semispan, large differences exist. Comparing the out-of-formation (lead) to the in-formation un-trimmed case, the shock is slightly reduced in strength and moves upstream due to the fact that the in-formation aircraft flies at an overall lower angle of attack. This is a result of the increased suction peaks seen in the in-formation configurations. When the trail aircraft is then roll-trimmed (in-formation aileron deflected to about -1.8 degrees), this shock is further decreased in strength and migrates further upstream of the deflected aileron.
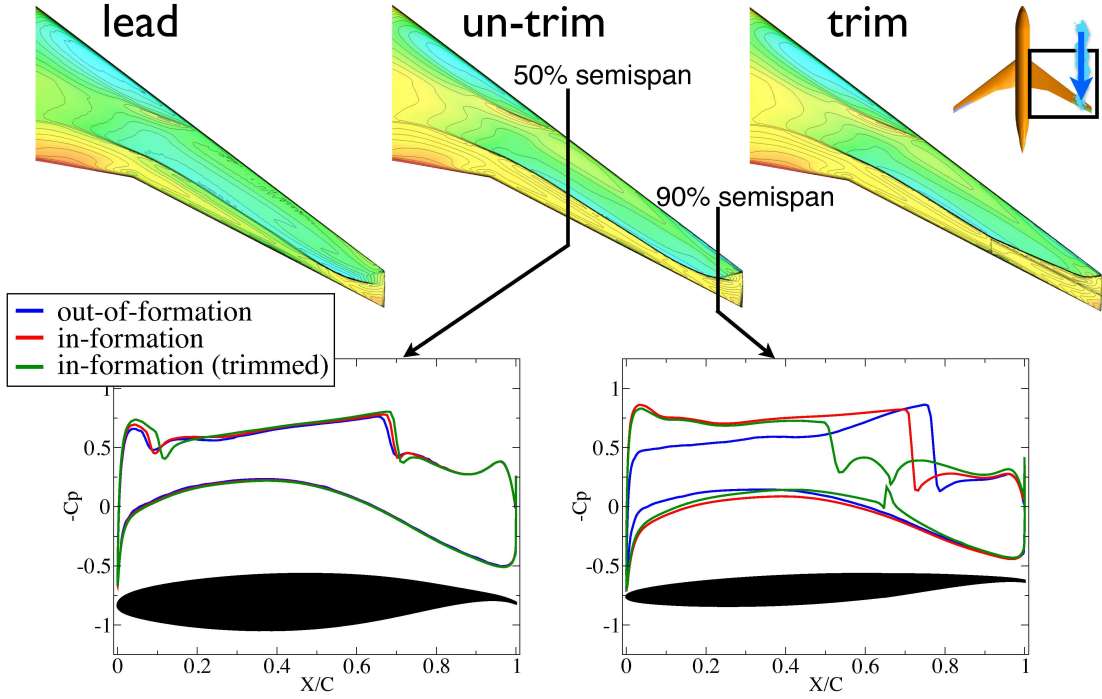

Figure 21: Surface pressures on in-vortex wing as a function of the aircraft configuration, along with C_P distributions at 50 and 90% semispan, respectively. The right aileron is deflected upward to counter the rolling moment of the incoming vortex. The incoming vortex is positioned at the wing tip.

Figure 22 displays the out-of-vortex wing of the CRM at Mach Number of 0.83, $C_L = 0.5$ for the three different flight configurations. Again, minor differences exist in the C_P distributions at 50% semispan. At 90% semispan, the out-of-formation, and in-formation (un-trimmed) configurations show little difference. As the out-of-vortex aileron is deflected downward to about 1.8 degrees to trim in roll, the shock is increased in strength, and migrates further aft on the aileron. Interestingly, the stronger shock appears on the out-of-vortex wing rather than the wing directly in the vortex. This very strong shock could be a potentially damaging effect if control surface buffet, or shock induced flow separation were to occur.
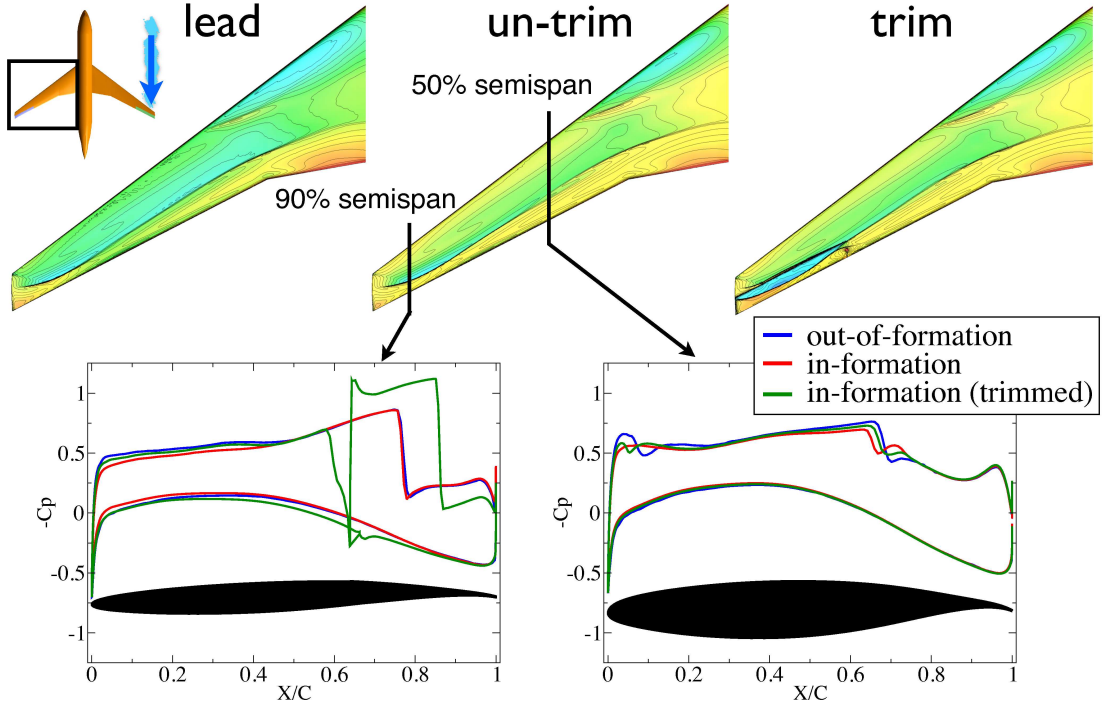
Figure 22: Surface pressure distribution on out-of-vortex wing as a function of Mach Number along with C_P distributions at 50 and 90% semispan, respectively. The left aileron is deflected downward to counter the rolling moment of the incoming vortex.

Figure 23 shows contour plots on the out-of-vortex wing as a function of Mach number for the roll-trimmed configuration, along with Cp distributions along the wing at 50% and 90% semispans. At Mach number of 0.79, the main wing (as shown previously) at 50% semispan is essentially shock free. As the Mach number is increased to 0.85, a shock forms on the main section of the wing which increases in strength and moves further aft.

At 90% semispan, the aileron has a strong shock on the aft portion for all Mach numbers. This strong shock on the aileron is a result of the aileron being deflected downward to trim in roll. As the Mach number is further increased, the shock moves further aft on the aileron. In terms of control surface buffet, or shock induced flow separation this could become a potentially hazardous situation and should be investigated in future work.
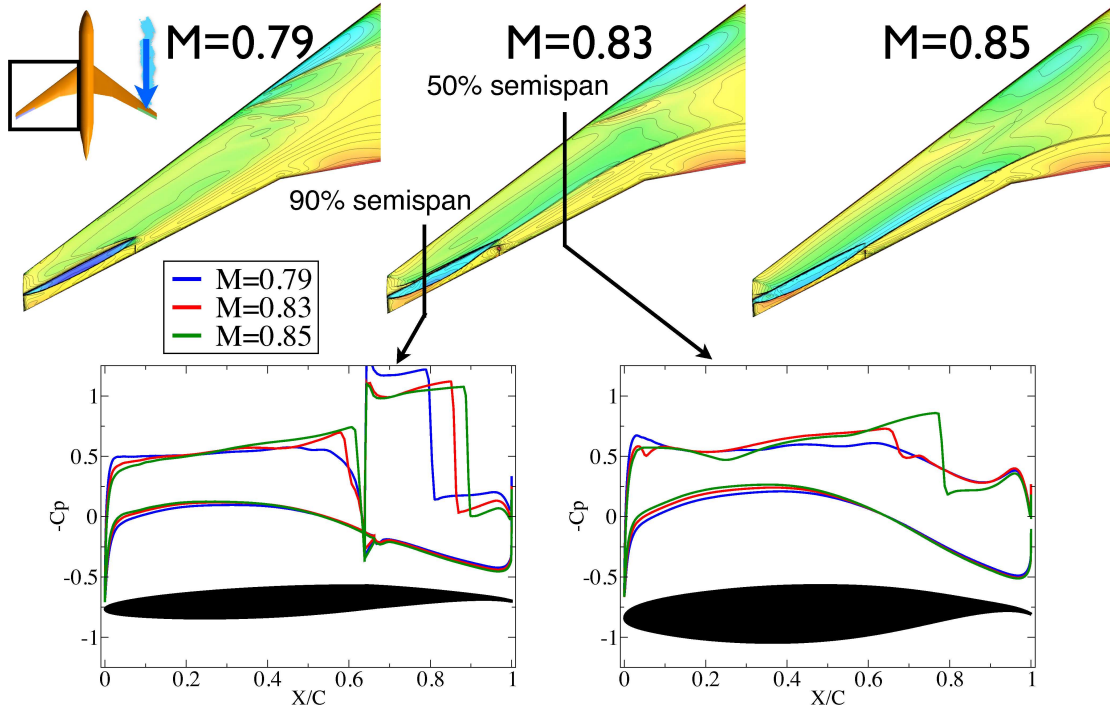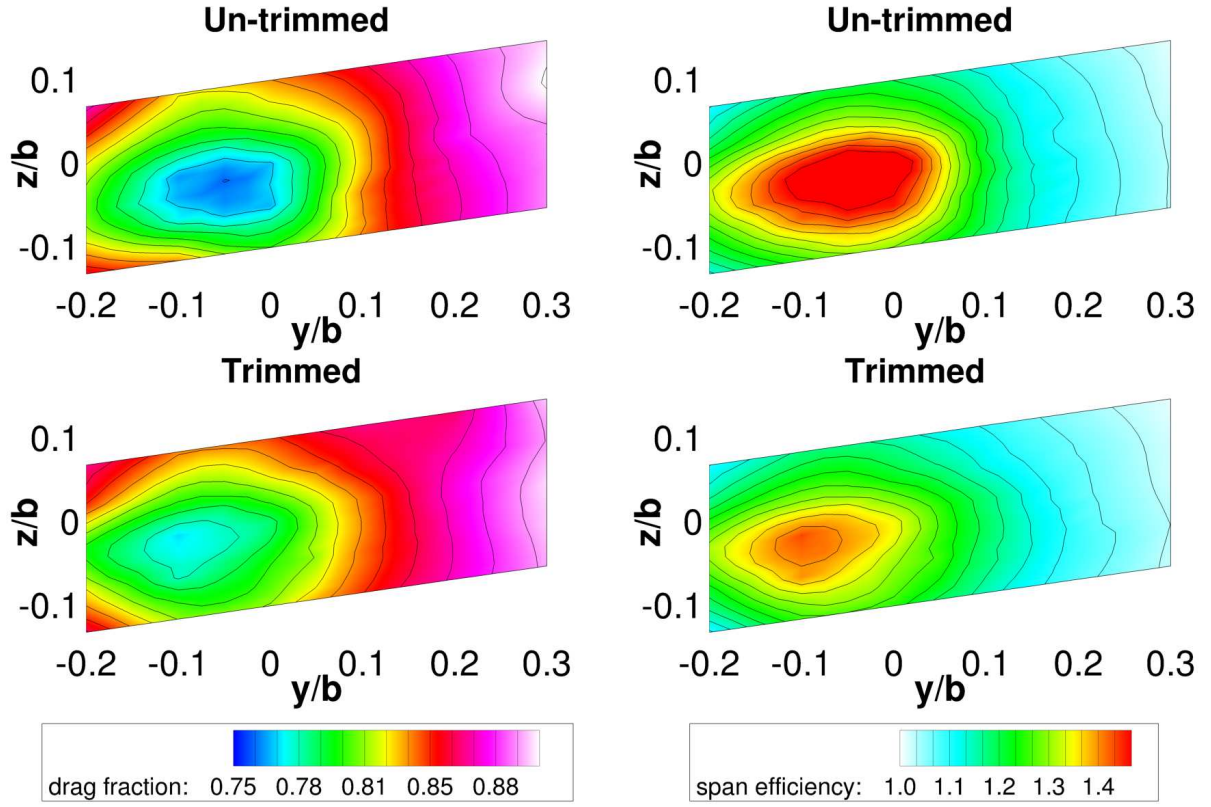
18

Figure 23: Surface pressure distributions on out-of-vortex wing as a function of Mach Number along with C_P distributions at 50 and 90% semispan, respectively. The left aileron is deflected downward to counter the rolling moment of the incoming vortex.

3.4.1 Vortex Position Sensitivity

A position sensitivity study similar to that in figures 12 - 17 was conducted for the CRM geometry extending from $y/b = -0.2$ inboard, and $y/b = 0.3$ outboard, with the vertical extent of $z/b = +/- 0.1$ of span. The contoured region is slanted to match the dihedral angle of the wing. Again, the origin of the coordinate system is at the wingtip. The CRM was run at a Mach Number of 0.84 for these cases by taking into account the results of Ning [13] to fly at a Mach Number 1-2% below the drag divergence Mach Number to reduce compressibility effects in formation. For all cases, the lift was held constant at $C_L = 0.5$. Figure 24 shows the contour maps of drag fraction along with span efficiency factor. The optimal position of the vortex with respect to the wing appears to occur around $y/b = -0.05$ wing overlap for the un-trimmed case. For the case of trim (using 2 anti-symmetric deflected ailerons) the optimal drag fraction and span efficiency migrates inboard toward $y/b = -0.1$. This is consistent with the results found for the simple subsonic wing as shown in figures 12 and 13.

(a) drag fraction

(b) span efficiency factor

Figure 24: Contour maps of (a) drag fraction and (b) span efficiency factor. For the un-trimmed configuration, the highest drag savings occurs near the wingtip with slight overlap (about 5%). This region migrates inboard (near $y/b = -0.1$ for the trimmed configuration) with roll-trim.

As in the simple wing results, the optimal positioning of the vortex appears to shift inboard with trim. At the optimal positions, trimming along with compressibility effects, reduce the maximum span efficiency factor by about 27% and increase drag fraction by 11%. In terms of trailing aircraft inviscid drag savings, a 50% savings is achieved without accounting for roll-trim, while a 35% savings is achieved with roll-trim. Therefore, roll-trim at transonic conditions results in a 15% erosion of formation flight inviscid drag savings on the trailing aircraft.

Figure 25 displays contour plots of rolling moment coefficients along with corresponding aileron deflection angles. Similar to the sub-critical wing results, the maximum rolling moments are occurring at the wingtip, and near the inboard boundary of the study. Additionally, there exists a region (white in the contour) where the rolling moments go to zero as in the sub-critical wing results. The corresponding aileron deflection angles (anti-symmetric deflection) reflect this behavior.

(a) rolling moment coefficient
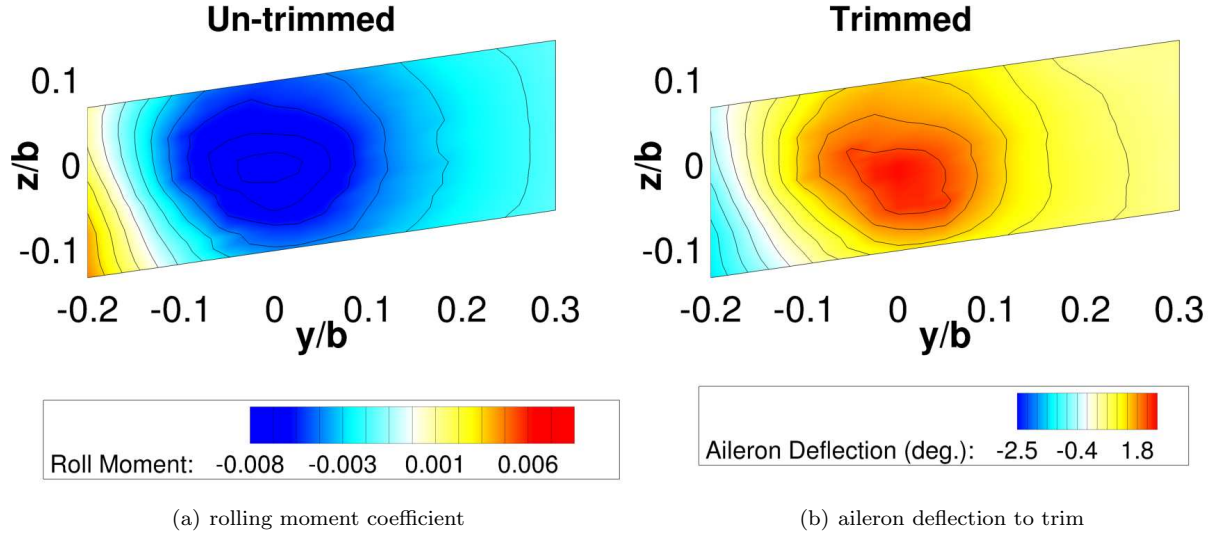
(b) aileron deflection to trim

Figure 25: (a) Rolling moment coefficients along with corresponding (b) aileron deflection angles. The largest rolling moments seem to occur at the $y/b = -0.2$ position and at the wingtip. The rolling moment changes sign as the vortex moves inboard as the wingtip within the vortex experiences more downwash and larger upwash inboard.

Conclusions

This paper examined the potential energy savings for extended formation flight quantified by span efficiency factor and drag fraction for two-aircraft echelon formations with a 30-span streamwise separation. Two crucial aspects of flying in formation are taken into account: trim and compressibility effects. An Euler solver combined with adaptive mesh refinement, and a wake propagation model were used to study two-aircraft echelon formations for both un-trimmed and trimmed configurations at fixed lift. A simple straight wing, along with a wing-body geometry were examined at both subsonic and transonic flight conditions for a matrix of vortex positions that spanned 20% of the span inboard and 30% outboard along the wing dihedral and +/- 10% in the vertical direction.

The results indicate that for subsonic flight conditions, the optimal vortex position occurs at the wingtip and migrates to about 10% overlap from the wingtip when the wing is roll-trimmed through aileron deflection. Drag fractions of at least 0.90 were found throughout the matrix of vortex positions analyzed. Sub-critical roll trim was found to account for a 3-5% increase in drag fraction (equivalently, an 8-10% reduction in span efficiency factor). In terms of inviscid drag savings on the trailing aircraft, roll-trimming in sub-critical flight conditions accounts for a 6% erosion of formation flight inviscid drag savings.

Simulations of transonic flow over a realistic wing-body showed the optimal vortex position exhibits qualitatively similar behavior to the simple wing geometry. Without trim, the optimal point occurs around 5% inboard from the wingtip and migrates along the dihedral to about 10% overlap with trim. Transonic trim was found to account for a 9-11% increase in drag fraction and a 25-27% reduction in span efficiency factor. In terms of inviscid drag savings, roll-trim at transonic conditions accounts for a 15% erosion of formation flight inviscid drag savings on the trailing aircraft. Overall, the trail aircraft saves 54% in induced drag subsonically, and 35% transonically when trimmed in roll.

Regions of zero induced rolling moment were detected (for both subsonic and transonic flight conditions) inboard around 10% of the wingtip indicating a theoretical point at which no control surface deployment would be needed to fly in formation and achieve close to optimal span efficiency. The conventional two-aileron deflection case proved to be most favorable in terms of induced drag reduction. This result is encouraging as it implies lower aileron deflections, as well as the ability to be implemented in today's aircraft without modification.

Some of the many challenges still to be faced before extended formation flight becomes a viable option include: sensing technologies to track the location of the vortex itself (and not just the lead aircraft), effects

of heterogeneous aircraft in formation, and more extensive flight testing at extended distances to better understand the physics involved. Additionally, control surface buffet, and shock induced flow separation in formation flight are potentially hazardous situations that need to be further explored.

Acknowledgments

References

[1] Lissaman, S., Shollenberger, C. A., *Formation Flight of Birds*, Science 168, 1003-1005. 1970.

[2] Hainsworth, B. Reed *Precision and Dynamics of Positioning by Canada Geese Flying in Formation*, Journal of Experimental Biology. 128, 445-462. 1987.

[3] Hummel, D., *Aerodynamic Aspects of Formation Flight in Birds*, Journal of Theoretical Biology, Vol. 104, No.3 1983

[4] Hummel, D., *Formation Flight as an Energy-Saving Mechanism*, Journal of Zoology, Vol. 41, No. 3, 1995, pp.261-278.

[5] Wagner, G., Jacques, D., Blake, W., and Pacher, M. *Flight Test Results of Close Formation Flight for Fuel Savings*, AIAA Paper, Vol. 4490, 2002.

[6] Vachon, M. J., Ray, R. J., Walsh, K. R., Ennix, K., *F/A-18 Performance Benefits Measured During the Autonomous Formation Flight Project*, NASA/TM-2003-210734. 2003.

[7] Bower, G. C., Flanzer, C., Kroo, I. M., *Formation Geometries and Route Optimization for Commercial Formation Flight*, AIAA paper 2009-3615, 27th AIIA Applied Aerodynamics Conference, Jun 2009, San Antonio, TX. 2009.

[8] Ning, S. Andrew, Flanzer, T.C., Kroo, I.M., *Aerodynamic Performance of Extended Formation Flight*, AIAA Paper 2010-1240, 48th Aerospace Meeting. Orlando, FL, Jan 2010.

[9] Ning, S. Andrew, *Aircraft Drag Reduction Through Extended Formation Flight*, Ph.D. Thesis, Department of Aeronautics and Astronautics, Stanford University, Aug 2011.

[10] Aftosmis, M., Berger, M., and Melton, J., *Robust and Efficient Cartesian Mesh Generation for Component-Based Geometry*, AIAA Journal, Vol. 36(6):952-960, 1998.

[11] Aftosmis, M., Berger, M., and Adomavicius, G., *A Parallel Multilevel Method for Adaptively Refined Cartesian Grids with Embedded Boundaries*, AIAA-2000-0808, 2000.

[12] Nemec, M., Aftosmis, M. J., *Adjoint Error Estimation and Adaptive Refinement for Embedded-Boundary Cartesian Meshes*, 18th AIAA Computational Fluid Dynamics Conference, Miami, FL, June 2007.

[13] Ning, S. Andrew, Kroo, I.M., *Compressibility Effects of Extended Formation Flight*, AIAA Paper 2011-3812, 29th AIAA Applied Aerodynamics Conference, June 2011.

[14] Aftosmis, M. J., Berger, M.J., *Adaptive Cartesian Mesh Generation*, Contributed chapter, CRC Handbook of Mesh Generation, 1998.

[15] Nemec, M., Aftosmis, M. J., and Wintzer, M., *Adjoint-Based Adaptive Mesh Refinement for Complex Geometries*, AIAA Paper 2008-0725, 46th AIAA Aerospace Sciences Meeting, Reno, NV, Jan 2008.

[16] Nemec, M., Aftosmis, M.J., Murman, S.M., and Pulliam, T.H., *Adjoint Formulation for an Embedded-Boundary Cartesian Method*, AIAA Paper 2005-0877, 43rd AIAA Aerospace Sciences Meeting, Reno, NV, Jan. 2005. (Also NASA Technical Report NAS-05-008.)

[17] Murman, Scott M., Chan, William M., et. al., *An Interface for Specifying Rigid- Body Motions for CFD Applications*, AIAA-2003-1237, Reno, NV, Jan 2003.

[18] Wintzer, M., *Span Efficiency Prediction Using Adjoint-Driven Mesh Refinement*, AIAA Journal of Aircraft, Vol. 47, No. 4, Jul-Aug 2010.

[19] Vassberg, J. C.,et al. *Development of a Common Research Model for Applied CFD Validation Studies*, AIAA Applied Aerodynamics Conference, AIAA 2008-6919, August 2008.